Environmental TEM study of electron beam induced electro-chemistry of $Pr_{0.64}Ca_{0.36}MnO_3$ catalysts for oxygen evolution

Stephanie Mildner[1], Marco Beleggia[2,3], Thomas Willum Hansen[2], Jakob Birkedal Wagner[2], Takeshi Kasama[2], Sadegh Yazdi[2], Jim Ciston[5], Yimei Zhu[4], and Christian Jooss[1]

[1] Institute of Materials Physics, University of Goettingen, Friedrich-Hund-Platz 1, 37077 Goettingen, Germany

[2] Center for Electron Nanoscopy, Danmarks Tekniske Universitet, Fysikvej (bygning 314) 2800 Kongens Lyngby, Denmark

[3] Helmholtz-Zentrum-Berlin fuer Materialen und Energie, Hahn-Meitner-Platz 1, 14109 Berlin, Germany

[4] Department of Condensed Matter Physics and Materials Science, Brookhaven National Laboratory, Upton, New York 11973, USA.

[5] National Center for Electron Microscopy, MS 72-150, Lawrence Berkeley National Laboratory, Berkeley, California 94720, Germany

Abstract

Environmental Transmission Electron Microscopy (ETEM) studies offer a great potential for gathering atomic scale information on the electronic state of electrodes in contact with reactants but also pose big challenges due to the impact of the high energy electron beam. In this article, we present an ETEM study of a $Pr_{0.64}Ca_{0.36}MnO_3$ (PCMO) thin film electro-catalyst for water splitting and oxygen evolution in contact with water vapor. We show by means of off-axis electron holography and electrostatic modelling that the electron beam gives rise to a positive electric sample potential due to secondary electron emission. The value of the electric potential depends on the primary electron flux, sample -conductivity and grounding, and gas properties. We present evidence that two observed electro-chemical reactions are driven by the beam induced electrostatic potential of the order of a volt. The first reaction is an anodic electrochemical oxidation reaction of oxygen depleted amorphous PCMO which results in a recrystallization of the perovskite structure. The second reaction is oxygen evolution which can be detected by the oxidation of a silane additive and formation of SiO_{2-x} at catalytically active surfaces. Recently published in-situ XANES observation of subsurface oxygen vacancy formation during oxygen evolution at a positive potential [32] is confirmed in this work. The quantification of beam induced potentials is an important step for future controlled electro-chemistry experiments in an ETEM.

1. Introduction:

Electro-catalysts are of high importance in speeding up electro-chemical reactions via the control of reaction steps and activation barriers [1]. Typically, electro-catalysts are used in the form of electrodes that enable the transfer of electrical charges into absorbed reactants. An ideal catalyst is not involved in the catalysed electro-chemical reaction. However, high catalytic performance typically requires materials with a sufficiently flexible atomic and electronic surface structure in order to affect the reaction processes [2,3]. In their active state, catalysts often undergo significant changes in surface and defect structure. A recent example even shows that a water splitting electro-catalyst can be formed during its activity [4]. Whether the catalyst forms desired highly active states, undergoes undesired changes which reduce its activity or even shows irreversible corrosion can sensibly depend on the specific ambient conditions. In-situ atomic scale studies of electro-catalysts in working conditions can contribute substantially to provide insights into the underlying mechanism [5,6].

Environmental Transmission Electron Microscopy (ETEM) studies using aberration corrected microscopes offer the opportunity for real space atomic resolution studies of catalysts at ambients of several mbar [7,8,9]. The high spatial resolution capabilities can be combined with a variety of analytical methods for chemical and band structure analysis by using local x-ray and electron energy loss spectroscopy [10]. The opportunity for real time observations of catalysts under close-by working conditions by a high-energy electron probe poses also a great challenge for well-defined studies of electro-chemistry due to the need for understanding and controlling the effect of the electron beam on the catalyst state.

Generally, the high energy beam electrons affect the studied sample via inelastic collisions with atoms and electrons. The appearance of atomic displacements is controlled by the ratio between the energy transfer of backscattered electrons to the atoms and their displacement energy E_d and thus is a function of the atomic mass and the energy of the primary electrons [11]. Point defect generation sets in above a threshold value of the primary electron energy which depends on the sample material. Above the threshold energy, the concentration of displacement generated defects increases with the electron dose. It is thus preferable for ETEM to ensure that the primary electron energy is appropriately selected in order to avoid beam induced defect generation.

In addition to atomic displacements, a variety of electronic excitations can be generated by the inelastic collisions of primary electrons with the electrons in the material. Inelastic scattering of high-energy electrons with band electrons can give rise to a variety of excitations such as plasmons [12], secondary electron emission [13] and even sample heating or point defect generation due to radiolysis [11] at high electron fluxes. Since electro-catalytic activity essentially depends on the electric potential of the catalyst, the effect of electrostatic charging due to the emission of secondary, core and Auger electrons must be addressed carefully. In fact, a beam-induced potential of the order of the redox potential of a catalysed chemical reaction may have a tremendous effect on the sample state. Understanding such effects quantitatively may allow for developing strategies towards controlled electro-chemistry in an ETEM.

Here, we present an ETEM study of a hole-doped $Pr_{1-x}Ca_xMnO_3$ (x=0.36) electro-catalyst with two well-characterized redox reactions: (i) Stable O_2 evolution at positive potential of V > 1.4 V versus Standard Hydrogen Electrode (SHE) at neutral pH in liquid electrolytes [14,15] and (ii) a reversible surface redox process at a potential of $V \sim 1$V versus SHE due to generation and annihilation of oxygen vacancies. Topotactic intercalation of oxygen at anodic currents just below the O_2 evolution potential is typical for many transition metal oxides [16,17]. The manganite catalyst represents an interesting model system for electro-catalysis of multi-step electron transfer reactions because of its flexible Mn valence state which may adjust to the different involved reaction steps.

In a previous study, we have shown that growth of SiO_2 from SiH_4 and H_2O at active PCMO areas is an indicator for O_2 evolution activity [17]. There, a beam-induced electro-chemical corrosion process in a Ca-rich PCMO sample has been stopped by applying a negative potential of $V \approx -1$V to the sample which was in good electrical contact with the biasing holder. In contrast to the previous study, the electron transparent PCMO/MgO lamellas for the present ETEM study are carefully cut by Focused Ion Beam (FIB) from PCMO thin films grown on MgO. The electrically insulating back contact in this geometry most likely results in higher beam-induced potentials. Despite of low energy Ar-ion post-milling a 1-3 nm thick oxygen depleted PCMO layer is rest on the sample surface that was used for the study of electro-chemical redox processes. Details on the sample preparation can be found in the supporting information S1. The selected sample geometry is suitable for systematic studies of the beam-induced electrostatic charging of the TEM lamella by off-axis electron holography. Recording the phase shift in vacuum near the sample edges at variable electron flux in combination with electrostatic modelling allows us estimating the amount of injected charge at steady-state conditions as well as the resulting beam induced electric potential.

2. Results

All ETEM studies presented have been performed with a 300 keV electron beam because it offers best high resolution imaging conditions in H_2O vapour environments. Fully oxidized PCMO shows high stability for 300 keV electrons under high vacuum conditions (typically 10^{-6} mbar or less). Even in high resolution STEM and EELS with electron fluxes as high as 10^{12} e/Å^{2}s, we have not found any indication of beam damage.

2.1 PCMO behaviour in pure water vapour

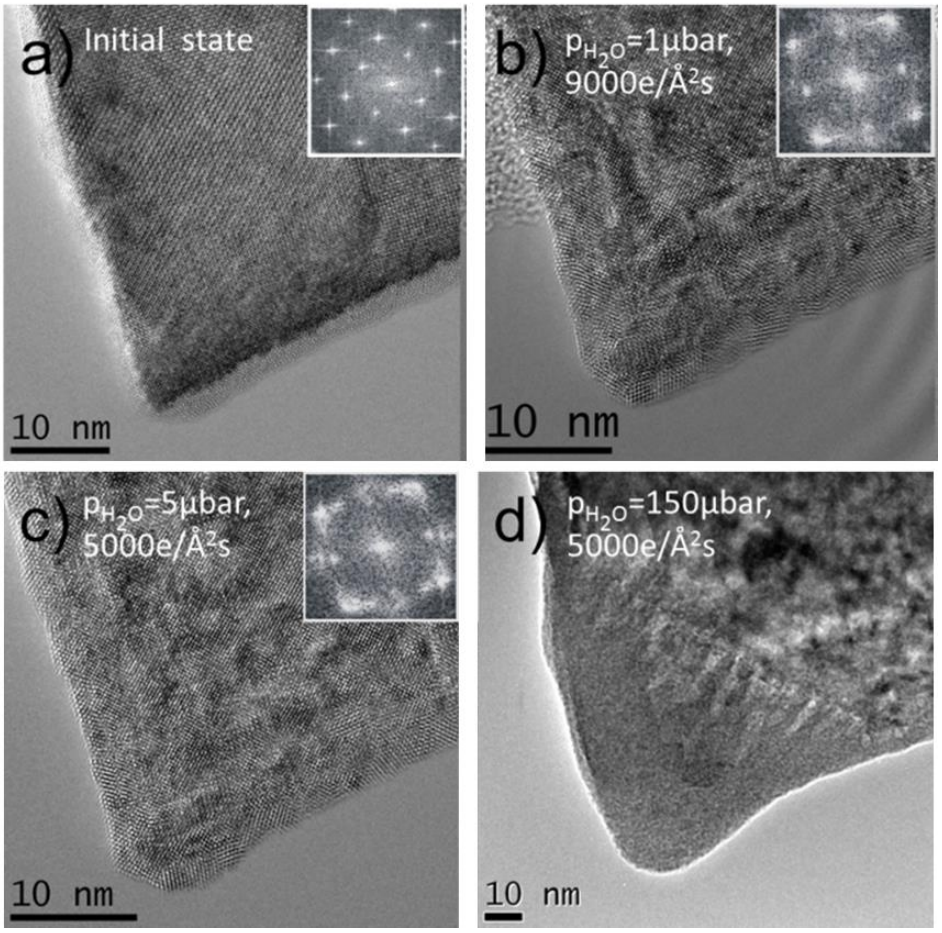

Figure 1: *HRTEM images of a crystalline edge of the PCMO film in different water pressure environments and electron fluxes. a) Initial state in high vacuum. b) State after 10 min in p_{H2O} = 1 µbar with electron flux of 9000 e/Å^{2}s. c) Same area 10 min after increasing the pressure to 5 µbar in a flux of 5000 e/Å^{2}s. d) Phase transition to amorphous state after enhancement of the pressure to 150 µbar at 5000 e/Å^{2}s. The insets show the corresponding diffractograms.*

The evolution of a crystalline edge of the PCMO film in contact with pure water vapour is depicted in Fig. 1. We have selected *a* ≈ 50 nm thick crystalline sample which is covered by a ≈ 3 nm thick amorphous surface layer of ion beam damaged amorphous PCMO. The thickness of the layer was measured under high vacuum conditions, where no changes due to the impact of the 300 keV electron beam were observed on time scales of 30 min. During the exposure to pure water vapour at a pressure of $p(H_2O)$ = 1 µbar and electron flux of 9000 e/Å^{2}s, the amorphous edges start to recrystallize. Recrystallization of thin amorphous areas also affects the surfaces with normal incidence to the electron beam as indicated by the inhomogeneous image contrast, while keeping a crystalline Pbnm structure (Fig. 1b). The corresponding Fourier transformed image (inset) shows that the initially sharp Bragg spots become spread. An enhancement of the pressure to $p(H_2O)$ = 5 µbar under exposure with

5000 e/Å^{2}s results in minor changes of the morphology of the recrystallized areas. Figure 1c shows the state after a total 20 min exposure to H_2O and the electron beam (10 min in $p(H_2O)$ = 1 µbar and 10 min in $p(H_2O)$ = 5 µbar, respectively). The HRTEM image reveals the existence of misoriented recrystallized domains with a size < 5 nm. The Fourier transformed image exhibits a further circle-shaped spreading of the Bragg spots as well as the appearance of some additional spots. These observations clearly indicate the formation of nanometer-sized crystalline domains with misorientation angles <30° (see the inset of Fig. 1c) by crystallization of the former amorphous areas of the sample.

Stability of the catalyst against beam-induced corrosion is only maintained for low water pressure. An increase of the pressure to $p(H_2O)$=150 µbar at 5000 e/Å^{2}s results in a phase transition to an amorphous structure in electron irradiated regions after a few minutes. Figure 1d is recorded after reestablishment of high vacuum. The observed processes stop when water vapour is absent. Thus, a recrystallization of initial amorphous edges via growth of misoriented nanocrystals requires water pressure of ~1 µbar whereas a pressure increase to >100 µbar results in amorphization of the former crystalline lattice. The interface between crystalline and amorphous material in Fig. 1d roughly corresponds to the boundary of the electron beam profile. Post characterization of the entire specimen confirms that such structural modifications only happen in regions exposed by the electron beam.

Electron energy loss near edge structure (ELNES) of the calcium L-edge, the oxygen K-edge and the manganese L-edge were measured in the initial state, after exposure to 5 µbar water vapour and after amorphization in 150 µbar water vapour (Fig. 2). The spectra of the O K-edge and the Mn L-edge are normalized to the intensity of the respective continuum excitation in a 5 eV window above the characteristic features. The Ca L-spectra are normalized to the L_2-peak intensity. The O K-edge (Fig. 2a) exhibits three sub-features labelled as A, B and C, which are well known for manganites. The pre-peak (feature A) arises from a hybridization of the O-2p states with the Mn-3d states. It basically reflects the hybridization of the O-2p with the e_g majority spin states and is sensitive to carrier doping and bonding characteristics. Feature B can be attributed to a hybridization with antibonding minority spin t_{2g} and e_g as well as Ca-d states. Feature C is related to hybridization with Pr, Ca, and Mn states at higher energy.

The O K-edge of the virgin sample shows an unusual small prepeak feature (A) compared to bulk PCMO TEM lamellas (thickness 70 nm) with the same doping level where amorphous surface material has been removed by low energy Ar-ion milling [18]. We attribute this to surface oxygen depletion, most likely caused by the sample preparation by means of FIB. Oxygen vacancies are known as electron donors filling the majority e_g-states in manganites. The exposure to low pressure water vapour ($\leq$ 5 µbar) results in an intensity increase of the O K-prepeak (A). This implies a depletion of majority e_g-states, i.e. an increase of hole doping. In contrast, subsequent exposure to 150 µbar water vapour results in a decrease of prepeak intensity to roughly the initial value, thus indicating oxygen depletion during amorphization. Furthermore a pronounced decrease of the intensity of feature C is obvious and denotes significant changes in the A-site cation configuration. This trend is confirmed by ELNES of the Ca L-edge. Typically, it is split into the L_3 and L_2-edge at 346 eV and 350 eV due to spin-orbit coupling of the Ca-2p states (Fig. 2b). Low pressure water vapour exposure does not induce any appreciable changes to the Ca L-edge. However, at 150 µbar water vapour, the L_3 intensity decreases drastically which indicates a change in the bond coordination [19, 20]. Changes in the ligand field can have a strong effect on the position and intensities of the L3 and L2 lines [21].The broad peak centred near 340 eV which evolves in high water pressure cannot be confidently assigned to the Ca L-edge, since different carbonates and sulphates with and without Ca can show such a signature [22].

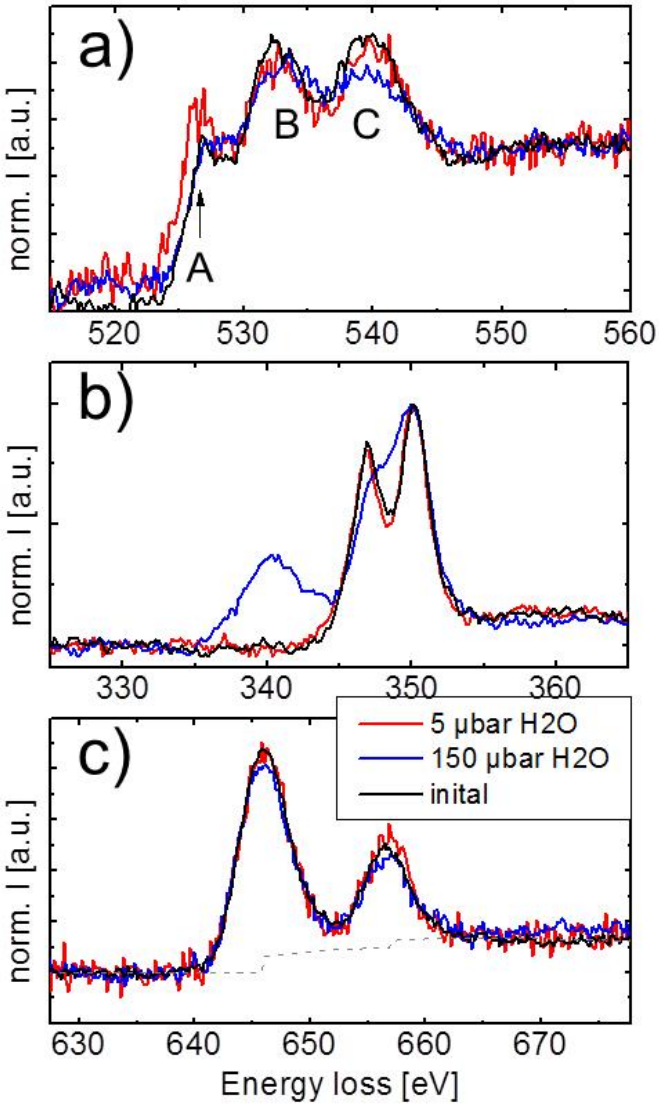

Figure 2: *Post mortem ELNES studies of the changes of characteristic loss edges after contact with water vapor. a) O K-edge, b) Ca L-edge and c) Mn L-edge. Initial state (black), after 5 µbar water exposure (red) and the amorphous state after 150 µbar water exposure (blue).*

Fig. 2c shows the Mn L_3 and L_2-edges (white lines) at 646 eV and 656 eV. We use the Gaussian fitting method for the determination of the $I(L_3)/I(L_2)$-intensity ratio, which is a measure for the Mn oxidation state [23] (for details see the supporting information S2). We find an initial $I(L_3)/I(L_2)$- ratio of 2.2. The resulting Mn valence state of +3.4 agrees with the nominal valence state expected from doping (+3.36). No significant changes of the L-edges are visible after 5 µbar water exposure, in contrast to the observation of an increased O K pre-edge. In comparison to the O K pre-edge, the Mn L-edge seems to be less sensitive to changes in the oxygen content of crystalline PCMO.

In contrast to the oxidation, the corrosive amorphization of PCMO during 150 µbar water vapour exposure results in visible changes both in the Mn L as well as in the O K edges. The increase of the Mn $I(L_3)/I(L_2)$-intensity ratio to 2.5 and indicates a decrease of the Mn valence to a value of +2.8. Simultaneously, the intensity of the O K pre-edge decreases and there is a signficiant reduction of the C peak which is due to hybridization of O and cation A sites. This change may indicate an incipient

decomposition of the PCMO perovskite manganite into other metal oxide compounds accompanied by a change in the Mn valence state.

2.2 Using SiO_{2-x} growth for monitoring catalytic activity of PCMO/MgO

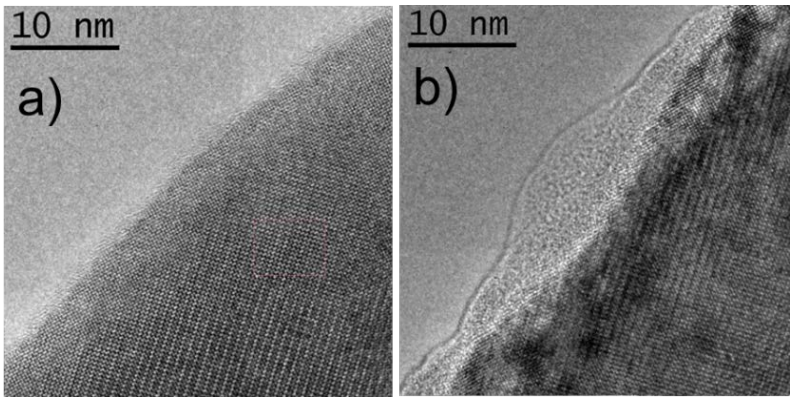

Figure 3: *Crystalline edge of the PCMO film (a) in vacuum and b) after t~120 s in H_2O/He/SiH_4 gas in an electron flux of 11000 e/Å^{2}s. The amorphous outgrowth in (b) represents SiO_2.*

Figure 3 demonstrates the development of a virgin sample region in 0.3 mbar of a H_2O/He/SiH_4 gas mixture with 1% H_2O vapour (p(H_2O)~3 µbar) during electron exposure with 11000 e/Å^{2}s. Figure 4a depicts the initial state with a crystalline edge. After a few seconds in gas the growth of amorphous material at the crystalline edges is observed. The state after 120 s in gas is shown in Fig. 4b. Using EELS and EDX spectroscopy, the amorphous outgrowth is identified as SiO_{2-x}. The growth of SiO_{2-x} is only observed under the following specific conditions:
i) It requires the presence of crystalline PCMO edges. If the same experiment is performed at amorphous PCMO edges or at catalytically non-active materials such as the copper sample support, no growth of SiO_{2-x} is observed.
ii) Exposing crystalline PCMO to the H_2O/He/SiH_4 mixture but without electron irradiation, the growth of SiO_{2-x} is absent. It is also absent if we move the electron beam away from the sample, where the high energy electrons interact only with the gas in the octagon. Consequently, the stimulation of the catalyst by the high energy electron beam is essential for the catalytic activity of PCMO in the TEM.
iii) SiO_{2-x} growth on PCMO requires water vapour, since neither structural modification in PCMO nor SiO_{2-x} growth is observed during the pre-characterization with electrons in high vacuum with the SiH_4 impurity. Since the SiH_4 gas is present even in high vacuum mode we thus can exclude a direct electron beam driven reaction between PCMO species and SiH_4.

These three observations are fully consistent with those reported by Raabe et al [17] for PCMO TEM lamella cut out of bulk material and show that SiO_{2-x} growth under these conditions can be considered as an indicator for oxygen evolution activity.

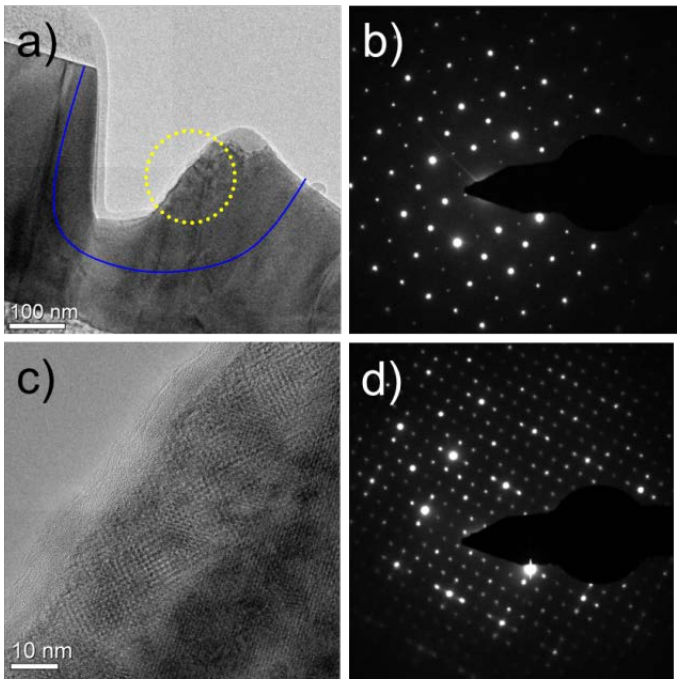

Figure 4: *Post mortem analysis of the induced changes in the PCMO film after the ETEM experiment in the 0.3 mbar H_2O/He/SiH_4 gas mixture. (a) TEM bright field overview image. The yellow circle marks the position of the electron beam with a flux of 11000 e/Å^{2}s.The diffraction pattern in (b) is measured in [001/110] zone axis immediately after return to HV mode and shows the initial structure. (c-d) During the post mortem study, a 2x2 superstructure starts to develop under the stimulation of the electron beam on a time scale of several minutes. (c) HRTEM image of the evolved superstructure. (d) The corresponding diffraction pattern of the area is shown in d). The blue line in a) marks the region with developed superstructure.*

Figure 4 summarizes the structural modifications of the PCMO after exposure to H_2O/He/SiH_4 and the electron beam. All images were gained in high vacuum mode after turning off the gas supply. An overview of the sample area after the reaction in gas is given in Fig. 4a. The yellow circle marks the position and size of the electron beam during presence of H_2O/He/SiH_4 gas. Visible changes of the PCMO crystal in the presence of gas, i.e. the deposition of amorphous SiO_{2-x} and the evolution of disorder are solely observed in electron irradiated regions and in their direct neighbourhood at a distance of ≈100 nm at maximum. While the PCMO crystal structure remains basically intact at the vertical edge regions, amorphization is observed above the primarily irradiated region at the horizontal edge (brighter top region above the yellow circle in Fig. 4a). Such horizontal edges suffer under strongly enhanced radiation damage during FIB preparation which may result in an increased instability against electrochemical corrosion during gas and electron exposure. These edges are not further considered in the analysis.

Diffraction patterns obtained of the electron and gas exposed region (Fig. 4b) do not reveal any significant changes compared to the initial state if studied immediately after the return to high vacuum (Fig. 4b). However, during the post-gas characterization a formation of a 2x2 superstructure is observed after a few minutes of electron exposure at a flux of 5000-25000 e/Å^{2}s (see Fig. 4c and d). The superstructure domains grow under the impact of the high energy electron beam. This phenomenon occurs only within regions that are close to the electron beam position during the ETEM gas experiment. The blue line in Fig. 4a depicts the borderline of the evolving superstructure domain. The image illustrates the final state after the growth of the superstructure domain has stopped even under further continuous electron beam irradiation. For verification purposes a crystalline region of PCMO far away from the reacted regions was exposed to electron beam for 10 min with the same

electron flux. It does not reveal any superstructure formation. This is consistent with our experience that virgin PCMO is rather stable against beam damage under HV conditions even under elevated dose rates.

Local ELNES spectra of the O K-edge and the Mn L-edge before and after the reaction in $H_2O/He/SiH_4$ gas (Fig. S2 in the supporting information) reveal a pronounced increase of the Mn $I(L_3)/I(L_2)$-ratio after the reaction. The disappearance of the O K-prepeak and the decrease of the Mn oxidation state from initially 3.3 to 2.4 after the reaction is in accordance with the observation of the formation of oxygen vacancies during the active state of PCMO bulk material [17]. We thus conclude that the 2x2 superstructure results from electron beam induced oxygen vacancy ordering (see discussion).

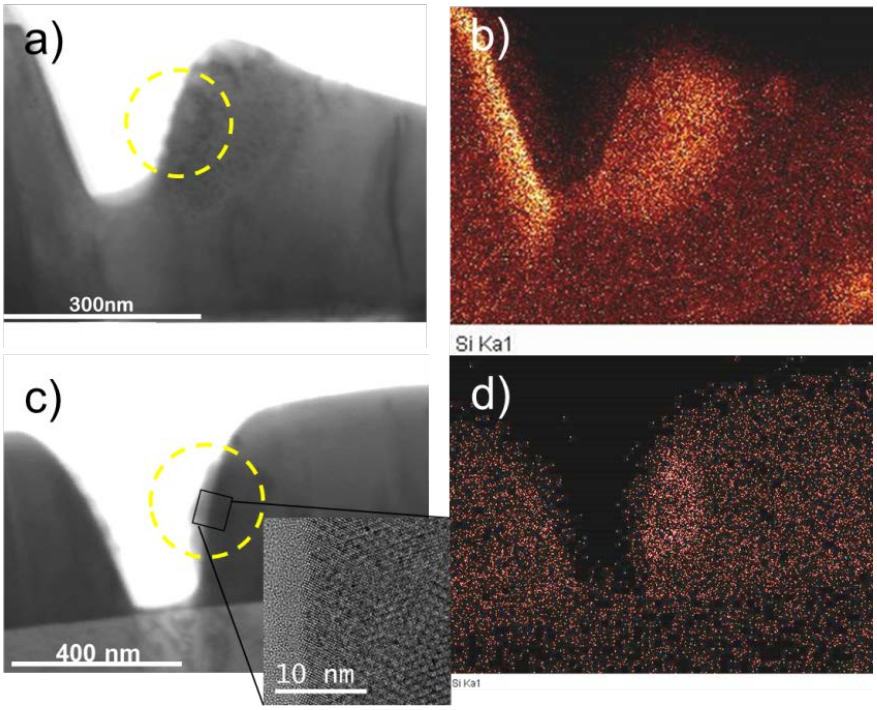

Figure 5: *Analysis of the effect of different electron fluxes on the oxygen evolution activity. a) A bright field STEM image of a reacted PCMO region (same region as depicted in Fig. 4 and 5) after electron irradiation with 11000 e/Å^{2}s in $H_20/He/SiH_4$ gas. The yellow circle marks the electron beam position and size during gas exposure. b) The corresponding EDX count map of the Si Kα1 emission shows maximum Si signal in regions adjacent to beam position. c) Bright field STEM image of another region of the same specimen which was treated under same conditions as the sample region depicted in a) but with decreased electron intensity of 2000 e/Å^{2}s. d) The corresponding EDX count map reveals a Si signal only in the primarily electron irradiated region.*

Figure 5 shows the SiO_{2-x} coverage of PCMO after exposure to 0.3 mbar gas mixture in and nearby electron-exposed areas at two different electron fluxes. The yellow circle marks the diameter of the electron beam during gas exposure. Fig. 5a shows a bright field STEM image of the sample region depicted in Fig. 4 after 15 min irradiation with 11000 e/Å^{2}s. The corresponding EDX-mapping of the Si-$K_{\alpha1}$ line in Fig. 5b reveals that significant Si concentration is present in and nearby the beam area. Remarkably, the area with Si coverage is found to be much larger than the initial beam size. Moreover, the maximum Si intensity is observed in areas outside the primarily electron exposed region, i.e. at the vertical edge of the next neighbour element as well as right to the beam area. Notably, the EDX-mapping shows that the regions where Si is found coincide with the regions exhibiting the 2x2 superstructure (see Fig. 4a). In all areas, where Si is found by EDX mapping, it exists in the form of SiO_{2-x} covering the PCMO sample as confirmed by EELS (not shown here).

Figure 5c and d show another sample area which has been exposed to the same gas mixture and pressure as before at a reduced electron flux of 2000 e/Å^{2}s for t~ 7min. Here, we also observe the growth of SiO_{2-x} as well as the formation of electron beam induced 2x2 superstructure during post-mortem analysis in HV (see inset of Fig 5c). In contrary to the experiment with 11000 e/Å^{2}s, EDX mapping in Fig. 5d shows a Si signal only in the area exposed to the electron beam. Only a marginal amount of 2x2 superstructure is observed at the neighbor edge left to the beam area.

3. Discussion

Our observations on the flux dependent local changes of the PCMO electrocatalyst and the active regions for the SiO_{2-x} formation as an indicator for oxygen evolution activity clearly show a major impact of the electron beam on the catalyst state. Oxidation accompanied by recrystallization of damaged amorphous PCMO areas and activity for oxygen evolution is induced by the electron beam if the catalyst is in contact with water vapour. This is a sign of a beam-induced positive electrostatic potential at the catalyst surface. In the following section we want to analyse in more detail the underlying processes. Based on off-axis holography and electrostatic modelling, we give an estimate of the induced sample potential and discuss the observations reported above in the light of the electro-catalytic behaviour.

3.1 Beam induced sample potential

(i) General theory

In contrast to SEM, where the absorption of primary electrons within insulating materials may often result in a negative sample charge [24], beam-induced potentials in TEM samples arise from the emission of secondary (SE), Auger (AE) and core electrons (CE). Altogether they produce a net flow of negative charges directed out of the sample which is partly compensated by backflow currents via groundings and environmental ionic gas species. All currents (emission and backflow) affecting the specimen charge are summarized in Fig. 6. The emission current is proportional to the beam primary current $I_e = I_p Y$, where the proportionality constant Y is the electron yield per incident electron. Y depends on the sample potential due to its effect on the escape probability. For simplicity, we only consider the SE contribution to Y, since the cross sections for generating AE and CE are much smaller than the SE generation. We estimate Y for SEs emitted from PCMO with energy E according to the equation of the yield spectrum $\frac{dY}{dE}$ given by Chung and Everhart [25], modified in order to taking into account the finite thickness d of the PCMO regions. The yield spectrum is calculated combining the probability (per unit primary path length) of generating a SE in the energy range $(E, E + dE)$ multiplied by the probability for such SE to reach the surface and escape into vacuum. The resulting spectral yield is given by

$$\frac{dY}{dE}(E,\phi) = 2 \cdot \frac{S(E)\lambda(E)}{4}\left(1 - \exp\left[-\frac{d}{\lambda(E)}\right]\right)\left(1 - \frac{E_F+\phi}{E}\right) \quad (1)$$

where ϕ is the work function of PCMO and E the energy of the SE relative to the bottom of the conduction band. The probability of beam induced electronic excitations in the specimen is described by $S(E) = C_Y/(E - E_F)^2$, where C_Y is a constant which depends on the energy of the primary electrons and material specific parameters. The factor 2 takes into account the existence of two surfaces, top and bottom surface of the PCMO lamella, where SE are emitted. Integration over all SE energies from vacuum level to infinity gives the total initial yield $Y_0 = 0.0034$ per primary electron of 300 keV for a 50 nm thick PCMO lamella. Details and diagrams regarding the calculation of the SE yield can be found in the supporting information S4.

As charges accumulate inside the sample and build up a potential V, it becomes increasingly difficult to extract further SEs since the escape barrier increases from ϕ to $\phi + eV$ and the yield decreases. The $Y(V)$ curve is obtained by

(2) $$Y(V) = \int_{E_F+\phi+eV}^{+\infty} dE \, \frac{dY}{dE}(E, \phi + eV)$$

Numerical evaluation of equation (2) followed by least-squares fitting of the $Y(V)$ curve to the model function $Y_0/(1+v)^{\beta}$, with $v = V/\phi$, results in $\beta \approx 2.2$ in the experimentally relevant interval $0 < v < 2$. The decrease of Y with V is the origin of a self-limiting process. In absence of the self-limitation, ithe sample potential would increase linearly with irradiation time in an insulator.
However, the self-limiting process does not fully saturate by itself, only changing the time dependence of the potential from linear to logarithmic, due to the power-law dependence of Y on V. Therefore, the establishment of a steady state with a "saturation" potential V requires a neutralization current I_n. In an ETEM, I_n can be comprised by two contributions: i) the current I_g from the ground through the sample holder into the TEM sample which depends on sample and contact resistances, and ii) the backflow current I_b originating from ionized gas species. Such ions can be generated in the gas environment either due to inelastic collisions of primary electrons with gas species or due to scattering and capture of SEs.
The accumulation of a charge q within the sample is governed by the continuity equation

(3) $$\frac{dq}{dt} = Y(V)I_p - I_n(V).$$

In the stationary state dq/dt =0, an equilibrium potential is evolving which is given by the intersection of the yield function $Y_0/(1+v)^{\beta}$ with the current ratio curve $I_n(v)/I_p$.

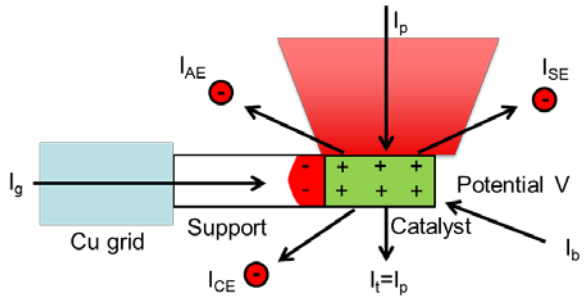

Figure 6*: Schematic representation of the generation of beam induced sample potential in a TEM lamella comprised of a semiconducting catalyst and an insulating dielectric support. Sample-beam configuration, where the high energy electron beam with intensity I_p is transmitting the semiconducting catalyst and is creating a positive charge by emission currents I_e of secondary electrons (SE), Auger electrons (AE) and core electrons (CE) due to inelastic scattering processes. In a stationary state, these emission currents are compensated by backflow I_b and ground currents I_g across the support. Note, the arrows describe the direction of the electron currents, not the conventional current direction.*

(ii) Beam induced potential from off-axis electron holography

Off-axis electron holography in combination with an approximate model of the potential distribution allows for a measurement of the beam-induced potential values at the PCMO surface. It is based on the determination of the phase shifts of electron waves which traverse a region interspersed by an electrostatic field or a magnetic potential. The phase shifts of the electron wave traversing the sample or near sample areas are measured by acquiring an interference pattern with a reference wave propagating far enough from the sample area in the vacuum. The position and contrast of the fringes in the gained interference pattern, the hologram, depend on the phase and the amplitude of the electron wave interacting with the specimen potential. The interference pattern is generated by placing a biased conductive wire (the biprism) at an appropriate location along the beam path, which acts as a beam splitter: half of the electron beam undergoes a phase shift due to interaction with the electric or magnetic fields of the specimen and the other half, ideally unperturbed, is the reference. In order to avoid phase shifts induced by a magnetic potential at the specimen area, the objective lens is switched off. Instead, a Lorentz lens is used which almost eliminates magnetic fields in the specimen region. Since our sample is paramagnetic, a possible magnetic potential from sample magnetization is absent,

too. Numerical image processing including Fourier transformations and filtering procedures of the hologram yields the phase as well as the amplitude image (see [26] for details).

A general relation between the electrostatic potential and the phase φ can be obtained by solving the Schrödinger equation describing an incoming plane electron wave propagating along the optical axis *z* through an electrostatic field given by -grad[*V*(*x*,*y*,*z*)]. Taking into account relativistic effects and neglecting dynamic diffraction as well as inelastic scattering, the phase modulation of the electron beam after passing through the sample is

(5) $$\varphi(x,y) = C_E \int_{-\infty}^{+\infty} V(x,y,z)\, dz$$

The constant C_E depends on the accelerating voltage of the used microscope: at 300 kV it has a value of C_E=6.53 rad/V μm. Within the sample interior, the phase shift originates from two contributions to the total electrostatic potential: the partially screened coulomb potential of the atomic nuclei (crystal potential) and the electrostatic potential generated by external charges induced by the beam. We aim at measuring only the second contribution. Consequently, we restrict the analysis of the phase shift to the outer areas of the sample, where the electrostatic potential distribution due to the stray field of the sample can be visualized.

Fig. 7a shows the phase shift $\varphi(x,y)$ which is obtained from an acquired hologram at a flux of 80 electrons/Å^{2}s. The gradient of the phase shift in the vacuum area near the sample edge increases with the used electron flux. (see Fig.S3 in the supporting information). Since the effect of the magnetic potential on the electron wave can be disregarded, the dependence of the phase gradient in the vacuum area near the sample reflects the electric potential distribution due to the beam induced surface charges of the TEM sample.

(iii) Modelling of the phase shift

In order to understand the observed phase shift $\varphi(x,y)$and to obtain an estimate of the induced surface potential, we need to model the phase shift in the sample exterior. We note first of all that any charge within the PCMO region, or on its surface, will polarize the (insulating) MgO support, resulting in an induced charge density that also contributes to the phase shift. For simplicity, we assume that the dielectric constant of the support is large enough to result in metal-like behaviour, i.e. the induced charges are physically located at the PCMO-MgO interface, and their electrostatic field is that generated by an image (negative) charge positioned mirror-symmetrically with respect to the external (positive) charge (see Fig. 7b).

Due to the rather high conductivity of PCMO, we expect the PCMO surface to be equipotential, i.e. we expect that all induced charges reside on the outer surfaces *S*, with a charge density distribution $\rho(\mathbf{r})$ that maintains S equipotential. The self-consistent solution of Poisson's equation

(6) $$\nabla^2 V(\boldsymbol{r}) = -\frac{\rho(\boldsymbol{r})}{\varepsilon_0 \varepsilon}$$

with the appropriate boundary conditions for a surface S of a roughly hemicylindrical object of radius *R* and height *t* requires numerical treatment and cannot be used conveniently for fitting the data.

Therefore, we introduce a further approximation: we assume that the charge is uniformly distributed within S, and is mirrored by an image-charge distribution within the MgO support as sketched in Fig. 7b. With this particular choice of $\rho(\mathbf{r})$, the phase shift comes directly from integrating along the optic axis the equation linking charge density and potential according to Eq. (6) and carrying out the remaining integrations along *r* and θ. The result is

(7) $$< V >= V_S \sum_{m=0}^{+\infty} \frac{C_m}{(2m+1)^2}$$

where $V_S = Ne/(4\pi\varepsilon_0 R)$ is the potential that would be established if all the measured charge were distributed over a spherical surface of radius R, and the coefficients of the capacitance series are given as a sum of Chebyshev polynomials (see supporting information S6).

By superimposing the fields generated by two equal PCMO regions laterally displaced by a gap d=110 nm (as measured from the calibrated experimental data), and by assigning the values R=215 nm and a total charge of Q=210 electrons, we obtain the simulated phase image shown in Fig. 7d. The parameters R and Q were fitted from the phase profiles taken along the red and green lines in 7c and d and explained in more detail in paragraph S6 in the supporting information.. The final step in the analysis is to extract the potential. Note first that a detrimental side effect of the uniform-charge-density approximation is that the potential of the PCMO regions is not a constant any longer: it varies with the angle along the curved outer surface, as well as with angle and radius over the top and bottom planar surfaces of the PCMO regions. To reconnect with the "sample potential" V, we take an average of the surface potential, which yields the value V=1.6 V.

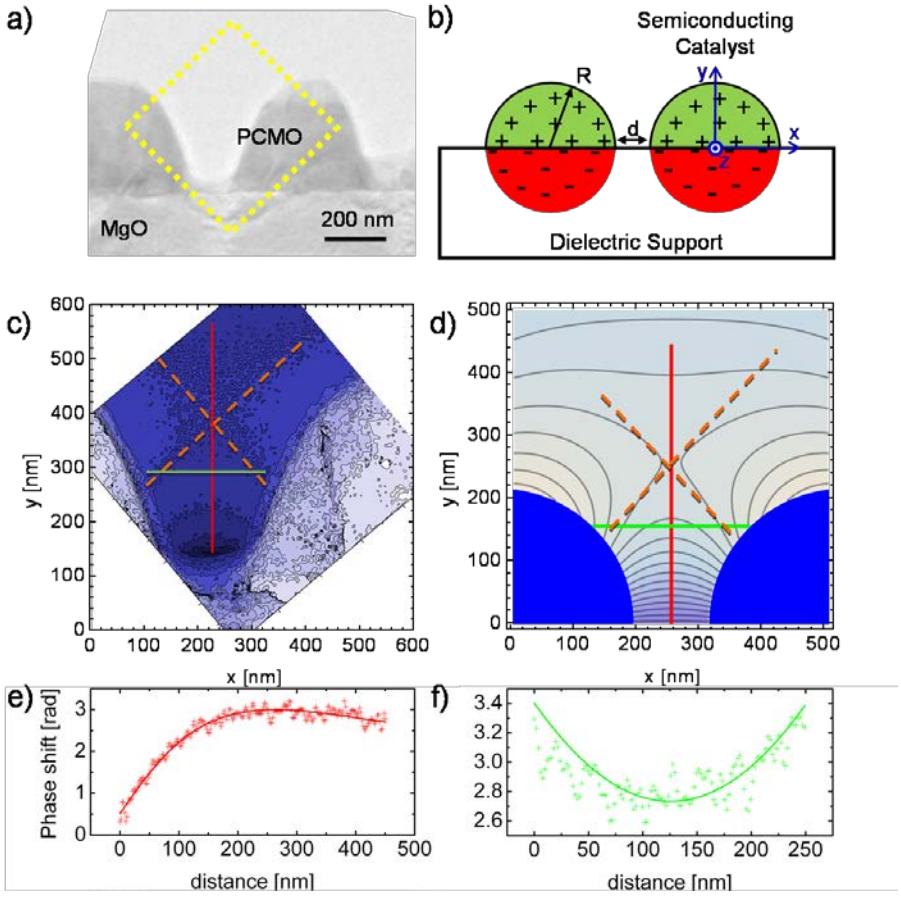

Figure 7: *Determination of the beam induced electric potential at the PCMO catalyst segments by off-axis holography and electrostatic modelling. (a) TEM image of the sample area used electron holography. (b) Simple model of the charge distribution within the catalyst / support structure, where the beam induced positive charges in the catalyst semi-cylinders with radius R and distance d are inducing negative counter charges within the dielectric support structure. (c) Contour map of the phase of the electron wave at an electron flux of ~80 e/Å^{2}s at the sample area marked in (a). (d) Contour map of the calculated phase shift around uniformly-charged semi-cylinders. Note the cross shaped pattern (saddle point in the potential) indicated by the broken orange lines and which is also visible in c). (e-f) Fit of the measured phase shifts along the green and*

red lines depicted in (c) and (d) resulting in R=215 nm, Q=210 electrons and an averaged (over the rim) surface potential of V_0=1.6V.

(iv) Comparison of ETEM and holography experimental conditions

For the comparison of beam induced potentials determined by holography under HV conditions with beam induced potentials under ETEM conditions, the continuity equation (Eq. 3) gives a very straightforward approach: For simplicity, we assume an Ohmic neutralization current. Then, the balance-of-currents equation reads $v(1+v)^{\beta} = Y_0 I_p R/\phi$. Using $Y_0 = 0.0034$ and ϕ = 4.9 eV, a positive potential in the order of 1V at an electron flux of 11000 e/Å^{2}s requires a sample resistance of the order of R ≈ 10^{10} Ω. For a smaller sample resistance, for example if the sample is well connected to ground or when the ionization of the gas environment enables sufficiently high backflow currents, the potential saturates at smaller values. The opposite limiting case is represented by a floating sample with $1/R = 0$ (regardless of whether the material is metallic or insulating itself). In this limit, the saturation potential would logarithmically depend on the total irradiation time: no steady-state would be reached, leading possibly to either arc-discharges or dielectric breakdown. In all intermediate cases, a saturation potential at most of the order of the work function may be expected.
Using an Ohmic approximation, the potential would scale with the product of I_p and *R*. Comparing the measured positive potential of 1.6V under an electron flux of 80 e/Å^{2}s in the holography experiment in Fig. 7 at HV (~0.1 μbar) with the electron flux of 11000 e/Å^{2}s in the ETEM experiments (Fig. 1b) at 1 μbar H_2O, one would expect an one order of magnitude higher potential (see supporting information S6). However, such a sensitive dependence of the sample potential on the product I_pR as predicted by the Ohmic approximation seems to be questionable: From ref. [17] we know that the application of -1 V during in situ experiment at a pressure of 1.3 mbar He/H_2O mixtures can stop the corrosion process. Thus, the similar potentials observed in both different types of experiments points to a non-linear current-voltage behavior, where higher potentials due to enhanced SE emission are damped because of an increase of I_n.

3.2 Behaviour of the PCMO electro-catalyst under ETEM conditions
Based on our estimate of a beam induced positive potential of the order of 1 V (or higher), we assume that conditions for anodic behaviour of the electro-catalyst are present in our ETEM experiments. Dependent on the magnitude of the potential *V*, the water pressure and the damage state of the catalyst, two different oxidation processes can be induced at the catalyst-water interface: (i) Oxidation of damaged, oxygen depleted areas of the PCMO electro-catalyst and (ii) oxidation of H_2O and oxygen evolution. Both processes also may coexist.

(i) Oxidation and recrystallization of damaged amorphous PCMO areas
The observation of an electron beam induced recrystallization process of initially amorphous PCMO in pure water vapour at electron flux <9000 e/Å^{2}s (Figs. 1b and c) is the following interpreted as an electrochemical oxidation of oxygen depleted amorphous specimen regions driven by a beam induced positive electrical potential. EELS of the O K-edge shows the reestablishment of the (A) pre-edge feature which was strongly suppressed in the as-prepared state of the sample (Fig. 2a). This is consistent with the presence of oxygen deficiency in the as-prepared state, where surface oxygen vacancy donor defects have been generated by the Ar -ion milling process of the TEM lamella. Healing of such donor defects increases the hole concentration of the O2p-Mn3d valence band which is indicated by the increase of the OK (A) pre-edge feature. EELS of the Mn L-edge shows a tiny increase of the L_{23} ratio and thus a small valence increase which is also consistent with the healing of electron donor defects such as oxygen vacancies (see Fig. 2c).

The absence of the recrystallization of amorphous PCMO as well as the related changes in the O K and Mn L-edges in high vacuum experiments indicates that the presence of H_2O or H_2O-derived intermediates is required for the healing of the damaged regions. The formed recrystallized phase has the same orthorhombic perovskite crystal structure as the virgin crystalline regions.

Electrochemical oxidation/reduction by oxygen intercalation/deintercalation is observed in cyclic voltammetry for many transition metal oxides. The redox process can take place at room temperature at electrical potentials of the order of $V_0 \approx 1$ V [27,28], where the oxidation of electrodes by oxygen intercalation requires an anodic polarisation. The oxygen intercalation is topotactic in nature, if the reaction does not involve diffusive rearrangement of the host atoms. In perovskite-derived structures of transition metal oxides $ABO_{3-\delta}$, a reversible topotactic transformation between fully oxygenized and O-deficient structures is typically observed at electrochemical potentials V slightly below the potential $V_0(H_2O \rightarrow \frac{1}{2}O_2+H_2)$ for oxygen evolution [29]. Grenier et al. [29] attributed the high mobility of the oxygen to the surface formation of O^- ions from H_2O or OH^- species. The penetration of O^- from the electrode surface into the bulk, requires metal cations with variable valence state and where the charge transfer reaction $B^{(n+1)} + O^{2-} \leftrightarrow B^{n+} + O^-$ only requires a small charge transfer energy. In addition to the electrochemical transformation between crystalline structures of different oxygen stochiometry, topotactic transformations may also involve amorphous phases [30].

The observed recrystallization of amorphous PCMO accompanied by increase of the O K pre-edge and Mn valence state in our ETEM experiments is thus fully consistent with an electro-chemical oxidation process under anodic conditions, where the required positive potential is induced by the high energy electron beam. Our observation that the recrystallization is limited to a H_2O pressure range of some µbar and changes into a beam induced amorphization / corrosion at higher H_2O pressure (Fig. 1d) is consistent with reduced electrostatic charging at increasing pressures in environmental electron microscopy [31]. A drop of the potential below the equilibrium potential for the oxygen intercalation would give rise to a reduction reaction of the electrode.

(ii) Electro-catalytic oxygen evolution indicated by the SiO_2 reaction

The growth of SiO_{2-x} at catalytically active surfaces in a $H_2O/He/SiH_4$ gas mixture at a partial pressure of $p(H_2O) \sim 3$ µbar is also consistent with the presence of a positive potential above 1 V. According to [17], SiO_{2-x} growth under such conditions indicates electro-catalytic oxygen evolution and cannot take place by a direct reaction of SiH_4 with H_2O. This statement is derived from the observation that the beam induced SiO_{2-x} growth requires the presence of a catalyst for oxygen evolution and does not take place at non-active materials or at amorphous PCMO edges. Cyclic voltammetry measurements reveal oxygen evolution at PCMO electrodes (x=0.34) at $V_{ox} > 1.4$ V (vs. SHE) at pH = 7. The formed oxygen can react with the SiH_4 molecules according to $SiH_4 + O_2 \rightarrow SiO_2 + H_2O/H_2$, with SiO_2 growing as a solid amorphous material on the catalyst surface.

The analysis of the Mn $I(L_3)/I(L_2)$-intensity ratio of EEL spectra yields a decrease of the Mn oxidation state in PCMO near SiO_{2-x} covered surfaces from 3.3 to 2.0. The Mn^{2+} formation at surfaces under oxygen evolution conditions is also observed by in-situ XANES experiments [32]. This valence decrease is consistent with the generation of oxygen vacancies and related electron doping while the crystalline perovskite structure is largely maintained.

Apparently, the oxygen vacancy formation under oxygen evolution conditions is contrary to the observation of oxidation of amorphous areas in experiments with pure H_2O vapour. Indeed, oxygen intercalation is often observed by cyclic voltammetry as an oxidation reaction preceding the oxygen evolution reaction. We assume that surface and subsurface oxygen vacancies participate in the O_2 evolution machinery. Consequently, the full oxidation of the catalyst may be not achievable after the oxygen evolution has set in. In [32] it is shown that the formation of oxygen vacancies in the active state of the PCMO catalyst is fully reversible and can be entirely healed out by at slightly elevated temperatures at zero bias.

The evolution of 2x2 superstructures in post mortem analysis of active catalyst areas is an additional strong argument for the presence of oxygen vacancies. Since the superstructures associated with charge order are only formed in the crystallographic b-direction and are mainly observed at low

temperatures [33], we can attribute the 2x2 superstructure at room temperatures in regions with reduced Mn valence and reduced O K pre-edge intensity to oxygen vacancy ordering. Furthermore, the time scale of superstructure formation under electron bombardment is of several minutes, indicating that vacancy redistribution or even diffusion is required to form the superstructure. We cannot exclude that in oxygen depleted sample areas additional oxygen vacancies can be generated by atomic displacements due to inelastic collisions of the primary electrons with oxygen atoms. The displacement energy E_d for oxygen atoms in perovskites is in the range of 45-55 eV [34,35,36]. The threshold energy for oxygen displacement is thus estimated to 260-320 keV for the primary electrons using Eq. (2) in Ref. [11]. Extensive studies of fully oxidized PCMO shows high stability for 300 keV electrons under high vacuum conditions, even at electron fluxes as high as 10^{12} e/Å^{2}s in STEM / EELS.

The appearance of large areas with increased oxygen vacancy concentrations raises the question, whether SiO_{2-x} was partially formed by the reduction of the electrode. Comparing quantitatively the amount of oxygen which is captured in the SiO_{2-x} layer with the amount of oxygen removed from the electrode to form a Brownmillerite phase is not possible. The SiO_{2-x} thickness spatially varies, and can only be estimated at those sample surfaces perpendicular to the electron beam. In addition, the oxygen content of the SiO_{2-x} may vary. In contrast to our observations at PCMO bulk samples, where catalytic turnover numbers of about 10 for oxygen evolution have been found [17], the turn over number for the PCMO thin film samples seems to be strongly reduced. We attribute this difference to sample damage such as preformed oxygen vacancies induced by FIB sample preparation. An increase of oxygen vacancies drastically increases the oxygen ion mobility in manganites [37]. This indicates a drop of the oxygen binding energy and thus higher sensitivity to high energy electron induced beam damage.

Nevertheless, the spatial extend of the area containing SiO_{2-x} measured by EDX and the appearance of the 2x2 superstructure in post mortem analysis as a function of the electron flux reflects interesting properties of the induced electric potential distribution. Increasing the electron flux from 2000 e/Å^{2}s to 11.000 e/Å^{2}s (Figs. 5b and d) without changing the beam diameter, strongly increases the area with SiO_{2-x} formation. Remarkably, the area of highest electron flux in the center of the electron irradiated area shows a significant reduction of the SiO_{2-x} growth compared to surrounding areas. This observation gives strong evidence that the spatial distribution of a sufficiently high positive potential for oxygen evolution can exceed the beam diameter by a factor which depends on the electron flux. Indeed, the area of post mortem 2x2 superstructure formation nicely corresponds to the area of SiO_{2-x} growth. The reduced SiO_{2-x} formation in the central beam area with the highest electron flux may either indicate that the local potential was too large or that beam damage may have reduced the reaction rate. We exclude that the spread of the SiO_{2-x} around illuminated areas is induced by beam spreading in gas, because the fraction of scattering events between primary electrons and gas atoms/molecules generally provoking a skirt-like beam spread [38] is very weak in the TEM due to small scattering cross section for 300keV electrons. Furthermore the largest SiO_{2-x} growth is always seen at the sample edges (see e.g. left edge in Fig. 5b) where the surface potential is highest.

4. Summary and conclusions

ETEM studies of a $Pr_{0.64}Ca_{0.36}MnO_3$ electro-catalyst in contact with water vapour reveal that two chemical reactions can be induced by the high energy electron beam: (i) The oxidation of oxygen depleted amorphous surface regions of the electrode which are formed during TEM sample preparation with FIB. The oxidation is visible in the increase of the O-K pre-edge feature and the formation of the Pbnm perovskite structure via recrystallization of the amorphous material. (ii) Oxygen evolution is detected via observation of the growth of SiO_{2-x} at catalytically active PCMO surfaces in a $He/H_2O/SiH_4$ gas mixture. We are aware that using SiO_{2-x} formation as an indicator for oxygen evolution is indirect. However, we base our conclusion on systematic ETEM studies which exclude a direct SiH_4 oxidation by water and show that an oxygen evolution catalyst is required. In accordance with a recent in-situ XANES study [32] which shows that reversible oxygen vacancy formation evolves at positive potentials under oxygen evolution conditions, we provide direct imaging

of the oxygen vacancy enriched areas by 2x2 superstructure formation combined to EELS of the oxygen K-edge. Although some of the SiO_{2-x} may be formed with oxygen from the electrode material, we can exclude that SiO_{2-x} growth is the origin of the oxygen vacancy formation.
Furthermore we conclude that whether PCMO electrodes surface and subsurface regions are oxidized or reduced in contact with water vapour may not only depend on the applied potential but rather seems to be an intrinsic property of the catalyst with respect to the oxygen evolution activity. Formation of Mn^{2+} and filling of the antibonding Mn e_g bands with more than one electron per unit formula would result in a reduced oxygen evolution activity as pointed out in ref. [39]
Based on the quantification of beam induced sample potentials by electron flux dependent measurement of phase shifts in off-axis holography, we present strong evidence that the observed chemical reactions are of electro-chemical nature, i.e. they are driven by a beam induced positive electrode potential of the order of 1-2 V. Electrostatic modelling provides insights into the balance of currents and thus into the conditions which are required for the build-up of potentials. The results show that potentials of the order of one volt can be easily built up in samples which are electrically insulated from the ground and in gas environments, where the ion and electron density is orders of magnitude below the generated charge density within the TEM sample. We are confident that the provided insights into the beam induced electric potential effects in ETEM will stimulate further experimental and theoretical work on measurement and control of electrode potentials and open up a pathway for controlled electro-chemical experiments under electron beam illumination.

---

[1] Jacek Lipkowski, Phil N. Ross, Electrocatalysis, John Wiley & Sons, 1998

[2] G. J. Hutchings, A. Desmartin-Chomel, R. Olier and J.-C. Volta, Nature 368, 41 - 45 (1994)

[3] L. Trotochaud, S. W. Boettcher, Scripta Materialia 74, 25-32 (2014)

[4] M. W. Kanan, D. G. Nocera, Science 321 (2008) pp. 1072-1075

[5] R. Arrigo, M. Hävecker, M. E. Schuster, C. Ranjan, E. Stotz, A. Knop-Gericke, R. Schlögl, Angewandte Chemie International Edition, 52, 11660–11664, (2013)

[6] F. Zheng, S. Alayoglu, J. Guo , V. Pushkarev, Y. Li, P.-A. Glans, J.-L. Chen, and G. Somorjai, Nano Lett., 11 847–853 (2011)

[7] L. Y. Chang, A. S. Barnard, L. C. Gontard, R. E. Dunin-Borkowski, Nano Lett. 2010, 10, 3073.

[8] P. L. Hansen, J. B. Wagner, S. Helveg, J. R. Rostrup-Nielsen, B. S. Clausen, H. Topsøe, Science 2002, 295, 2053.

[9] S. Helveg, C. López-Cartes, J. Sehested, P. L. Hansen, B. S. Clausen, J. R. Rostrup-Nielsen, F. Abild-Pedersen, J. K. Nørskov, Nature 2004, 427, 426.

[10] T. W. Hansen, J. B. Wagner, R. E. Dunin-Borkowski, Mater. Sci. Technol. 2010, 26, 1338.

[11] R.F. Egerton, P. Li, M. Malac, Micron 35 (2004) 399–409.

[12] P. Schattschneider and B. Jouffrey, Plasmons and Related Excitations, in: Energy-Filtering Transmission Electron Microscopy, Springer Series in Optical Sciences, 71 (1995) 151-224

[13] K. H. Downing, M. R. McCartney, R. M. Glaeser, Microsc. Microanal. 2004, 10, 783.

[14] Bockris, J.O.M. & Otagawa, T. The electrocatalysis of oxygen evolution on perovskites. J. Electrochem. Soc. 131, 290 (1984)

[15] Y.Matsumoto and E.Sato, Materials Chemistry and Physics, I4 (1986) 397-426

[16] J. –C. Grenier, M. Pouchard and A. Wattiaux, Current Opinion in Solid State and Materials Science 1 (1996) 233-240.

[17] S. Raabe, D. Mierwaldt, J. Ciston, M. Uijttewaal, H. Stein, J. Hoffmann, Y. Zhu, P. Blöchl, and Ch. Jooss, Advanced Functional Materials, 22 (2012) 3378–3388

[18] G Saucke, J. Norpoth, Ch. Jooss, D. Su and Y. Zhu, Phys. Rev. B 85, 165315 (2012).

[19] Montenegro, M. J.; Lippert, T.; Müller, S.; Weidenkaff, A.; Willmott, P. R.; Wokaun, A. Appl. Surf. Sci. 2002, 197-198, 505-511.

[20] Montenegro, M. J.; Döbeli, M.; Lippert, T.; Müller, S.; Schnyder, B.; Weidenkaff, A.; Willmott, P. R.; Wokaun, A. Phys. Chem. Chem. Phys. 2002, 4, 2799-2805.

[21] F. M. F. de Groot, J. C. Fuggle, B.T. Thole and G. A. Sawatzky, Phys. Rev. B 41 (1990) 928.

[22] M. T. Costelloa, and M. Kasraib, Tribology Letters, 24 (2006) 163-169

[23] T. Riedl, T. Gemming, K. Wetzig, Ultramicroscopy 106 (2006) 284–291

[24] Toth, M., Phillips, M., Craven, J., Thiel, B. & Donald, A. Electric fields produced by electron irradiation of insulators in a low vacuum environment. J Appl Phys 91, 4492–4499 (2002)

[25] M. S. Chung and T. E. Everhart, J Appl Phys 45, 707 (1974);

[26] A. Tonomura. Rev. Mod. Phys., 3, 639 (1987).

[27] A. Nemudry, P. Rudolf, R. Schöllhorn, Chem. Mater. 1996, 8, 2232.

[28] S. Bakardjieva, P. Bezdička, T. Grygar, P. Vorm, J. Solid State Electrochem 2000, 4, 306.

[29] Jean-Claude Grenier, Michel Pouchard, Alain Wattiaux, Electrochemical synthesis: oxygen intercalation, Current Opinion in Solid State and Materials Science, 1 (1996) 233-240

[30] J. Kim & A. Manthiram, A manganese oxyiodide cathode for rechargeable lithium batteries, Nature 390, 265-267

[31] Athene M. Donald, The use of environmental scanning electron microscopy for imaging wet and insulating materials, Nature Materials 2, 511 - 516 (2003)

[32] D. Mierwaldt, S. Mildner, R. Arrigo, A. Knop-Gericke, E. Franke, A. Blumenstein, J. Hoffmann, C. Jooss, acctepted for publication in Catalysts (2014)

[33] L. Wu, R. Klie Y. Zhu, and Ch. Jooss, Phys. Rev. B 76 (2007) 174210Wu et al, PRB…

[34] K. L Smith, M. Colella, R. Cooper, E. R. Vance, Journal of Nuclear Materials, 321, 2003, Pages 19–28

[35] S.B. Ubizskii, A.O. Matkovskii, N. Mironova-Ulmane, V. Skvortsova, A. Suchocki, Y.A. Zhydachevskii, and P. Potera, phys. stat. sol. (a) 177 (2000) 349

[36] B.S. Thomas, N.A. Marks and B.D. Begga, Nucl. Inst. and Meth. in Phys. Res. B: 254, 2007, Pages 211–218

[37] oxygen mobility in oxygen deficient perivskites;LOOK FOR LITERATURE

[38] S.A. Wight, Scanning 23.5 (2001): 320-327.

[39] J. Suntivich, K. J. May, H. A. Gasteiger, J. B. Goodenough, Y. Shao-Horn, *Science* **2011**, *334*, 1383.